Final Technical Report

Project Title: "Optimization of concentrator photovoltaic solar cell performance through photonic engineering"

Project Period: 10/01/2016 to 12/31/2017

Project Budget: Oct 1, 2016 to Sept 30, 2018

Submission Date: 03/30/2018

Recipient: The Leland Stanford Junior University

Address: Stanford, CA 94305

Award Number: DE-EE-0007544

Project Team: Stanford University and the National Renewable Energy Lab

Contact: James Harris
Professor
Phone: 650-723-9775
Email:jharris@stanford.edu

DOE Contacts:	DOE Contracting Officer:	Christopher Anderson
	DOE Technical Project Officer:	Inna Kozinsky
	DOE Technology Manager:	Rebecca Jones Albertus

Executive Summary:

The efficiency of state-of-art concentrator photovoltaic (CPV) solar cells has increased significantly over the last decade. However, the DC average efficiency of modules is only ~30%, a far greater disparity between cell and module efficiency than for flat plate Silicon. This gap between cell and module efficiency is largely due to daily and seasonal spectral variations, optical losses in the optics and increased operational temperature. Module components serving to minimize these losses significantly increase the cost of modules and have limited their large-scale deployment.

The goal of this program was to incorporate two new and innovative design concepts into the design and production of CPV cells that have near zero added cost, yet significantly increase the operational efficiency of CPV modules. The program focused developing luminescent coupling effects and radiative cooling layers to increase efficiency and suppress CPV module power losses due to spectral variations and heating.

The major results of the program were:

1) The optics of three commercial refractive (Fresnel) concentrators were characterized and prevent application of radiative cooling concepts due to strong mid-IR absorption (4-12μm) required to effectively radiate blackbody radiation from the cells and provide cooling. Investigation of alternative materials for the concentrator lenses produced only undesirable options—materials with reasonable mid-IR transmission for cooling only had about 30-40 visible transmission, thus reducing incident sunlight by >50%. While our investigation was somewhat limited, our work suggests that the only viable concentrator system that can incorporate radiative cooling utilizes reflective optics.
2) With limited ability to test high concentration CPV cells (requires outdoor testing), we acquired both semi-crystalline and crystalline Si cells and tested them in our outdoor facility and demonstrated 4°C cooling using a simple silica layer coating on the cells.
3) Characterizing Si cells in the IR associated with radiative cooling, we observed very significant near-IR absorption that increases the cell operating temperature by a similar amount, 4-5°C. By appropriate surface layer design, one can produce a layer that is highly reflective in the near-IR (1.5-4μm) and highly emissive in the mid-IR (5-15μm), thus reducing cell operational temperature by 10°C and increasing efficiency by ~1% absolute. The radiative cooling effect in c-Si solar cells might be further improved by providing a higher thermal conductive elastomer for securing the cover glass on top of the AR-coating. Since it was never imagined that the front surface would provide any cooling for solar cells, thermal conductivity of this elastomer was never a design consideration, but, improving the conductivity could decrease cell temperature by another 3-4°C. The combined effect could be an ~1.5% absolute increase in cell and module efficiency, a very significant improvement.
4) Developed a numerical model to explore dependence of luminescent coupling efficiency over a broad range of operating conditions. We developed a novel method and facility to experimentally measure the luminescent coupling that can be used to confirm the dependence of luminescent coupling on multi-junction cell design parameters.

Table of Contents **Page**

I. Project Results and Discussion

A. Luminescent Coupling Results and Discussion

The main results on luminescent coupling can be summarized in two parts:

1. We built a numerical model to explore dependence of luminescent coupling. The model can be used to predict the luminescent coupling efficiency under various operating conditions.
2. We developed a novel method to experimentally measure the luminescent coupling, which can be used to confirm the dependence of luminescent coupling.

1. Numerical model for luminescent coupling

We conducted the study based on a GaAs/InGaAs dual junction cell, which corresponds to the middle and bottom junctions of an IMM 3J solar cell. Our model contains two parts: optical and electrical transport models. In the optical part, optical generation distribution was originally simulated with AM 1.5 D and modified with the effect of photon recycling (PR) and luminescent coupling (LC). In the electrical transport model, calculated optical generation in the optical model was used to determine photocurrent through cell with different bias voltage.

a. Optical model

In this article, we utilized the well-studied optical redistribution matrix method to take photon recycling and luminescent coupling into account. To simplify the analysis, we conducted the study based on a dual junction model. The initial optical generation was simulated with the AM 1.5 D spectrum both in the top and bottom junctions. Due to the significant larger width of the device (millimeter scale) compared with its thickness (micrometer scale), the model was simplified into one dimensional simulation. Redistribution of photons emitted from top junction due to radiative recombination and absorbed throughout the cell is first modeled with Lumerical FDTD^{TM}. As the cell was meshed into layers in the simulation, the optical redistribution matrix was generated based on the layers generated during the FDTD simulation. Diploe light sources were placed on each mesh points of the structure and optical absorption was calculated. The result showed good agreement with the absorption equation:

$$I(d) = I_0 \exp(-\alpha d) \tag{1}$$

where $I(d)$ is the intensity at the depth of d, I_0 is the origin light intensity at the depth of zero, and α is the monochromatic absorption coefficient. The optical redistribution can be expressed in the form of $P(x)$:

$$P(x) = P_{sun}(x) + \sum_{y_{top}} P_{PR,top}(x, y_{top}) \tag{2}$$

for the top junction, and:

$$P(x) = P_{sun}(x) + \sum_{y_{bot}} P_{PR,bot}(x, y_{bot}) + \sum_{y_{top}} P_{LC}(x, y_{top}) \tag{3}$$

for the bottom junction.

Here $P(x)$ is the photon distribution at x^{th} mesh, $P_0(x)$ is the origin photon distribution from solar irradiance, $\sum_{y_{top}} P_{PR,top}(x, y_{top})$ and $\sum_{y_{bot}} P_{PR,bot}(x, y_{bot})$ is the total additional photon generated in each y^{th} mesh within the top or bottom junction contributing to

$P(x)$, $\sum_{y_{top}} P_{LC}(x, y_{top})$ is the sum of additional coupling photon generated in top junction contributing to $P(x)$ in the bottom junction. We used the subscript y_{top} and y_{bot} to discriminate the mesh of different junction.

$P_{PR,top}(x, y_{top})$, $P_{PR,bot}(x, y_{bot})$ and $P_{LC}(x, y_{top})$ can be calculated by multiplying $P_{sun}(y)$ with the matrix *M(y, x)* which described the possibility of a photon emitted from y^{th} mesh and was absorbed at x^{th} mesh.

b. Electrical transport model

With the optical generation and photon distribution simulated in each junction, carrier generation and recombination rates were simulated. The photocurrent density can be expressed as:

$$J_{ph} = J_{opt} - J_{rec} \tag{4}$$

Here J_{ph} is the photocurrent density, J_{opt} is the integrating of optical generation rate, and J_{rec} is the integrating of recombination rates:

$$J_{opt} = \int -qG(x)dx \tag{5}$$

$$J_{rec} = \int -qR(x)dx \tag{6}$$

In particularly, the optical generation the top junction and bottom junction can be expressed in form of different sources:

$$G_{top}(x) = G_{sun,top}(x) + G_{PR,top}(x)$$

$$G_{bottom}(x) = G_{sun,bottom}(x) + G_{PR,bottom}(x) + G_{LC,bottom}(x)$$

Here $G_{top}(x)$ and $G_{bottom}(x)$ are the optical generation rate in top and bottom junction, $G_{sun,top}(x)$ and $G_{sun,bottom}(x)$ are the optical generation due to incident light, $G_{PR,top}(x)$ and $G_{PR,bottom}(x)$ are the optical generation due to photon recycling, $G_{LC,bottom}(x)$ is the optical generation due to luminescent coupling.

The recombination rate can be expressed as:

$$R_{top} = R_{Rad,top} + R_{non-Rad,top} \tag{7}$$

$$R_{bottom} = R_{Rad,bottom} + R_{non-Rad,bottom} \tag{8}$$

Here R_{top} and R_{bottom} are the total recombination rate, $R_{Rad,top}$ and $R_{Rad,bottom}$ are the radiative recombination rate, and $R_{non-Rad,top}$ and $R_{non-Rad,bottom}$ are the nonradiative recombination rate. Here we assumed SRH recombination to be the dominant non-radiative recombination mechanism and neglect other recombination mechanisms such as Auger recombination.

According to the definition of luminescent coupling efficiency (LCE):

$$\eta = \frac{J_{LC,bottom}}{J_{rec,top}} = \frac{\int -qG_{LC,bottom}(x)dx}{\int -qR_{top}dx} = \frac{\int G_{LC,bottom}(x)dx}{\int R_{top}dx} \tag{9}$$

Here $J_{LC,bottom}$ is the luminescent coupling current and $J_{rec,top}$ is the recombination current in top junction. We also introduce another important parameter, emission efficiency (EE), which is defined as the ratio between radiative recombination current and total recombination current in top junction. It plays an essential role in understanding and predicting the behavior of LCE under various conditions.

Since we attributed $R_{non-Rad}$ totally to R_{SRH},the radiative and non-radiative recombination rate in our model as well as their ratio can be expressed as.

$$R_{Rad} = B(np - n_i^2) \tag{10}$$

$$R_{SRH} = \frac{(np-n_i^2)}{\tau_p\left(n+n_i \exp\left(\frac{E_{trap}}{kT}\right)\right)+\tau_n(p+n_i\exp\,(\frac{-E_{trap}}{kT}))} \tag{11}$$

$$\frac{R_{Rad}}{R_{SRH}} = B\ \cdot(\tau_p\left(n+n_i \exp\left(\frac{E_{trap}}{kT}\right)\right)+\tau_n(p+n_i\exp\,(\frac{-E_{trap}}{kT}))) \tag{12}$$

where τ_p and τ_n are SRH minority carrier lifetimes of holes and electrons, and B is the radiative recombination coefficient.

Note that the tunneling diode between the two junctions is carefully investigated and turns out to only act as a series resistance, consistent with previous simulation work. In this way, the tunnel diode will not influence the value of the LCE.

The simulation algorithm is summarized in Fig. 1. Simulations of the two junctions was conducted separately while the constrain to link them together is the continuity of photocurrent through two junctions. To determine the whole J-V curve, simulation started with an assuming-valid voltage V_{top} across junction 1 starting from open circuit voltage. An initial optical generation $G_{sun,\,top}$ from solar spectrum was simulated in Sentaurus TCAD v2012 and the corresponding photocurrent at the given voltage was obtained using Lumerical DEVICE™.

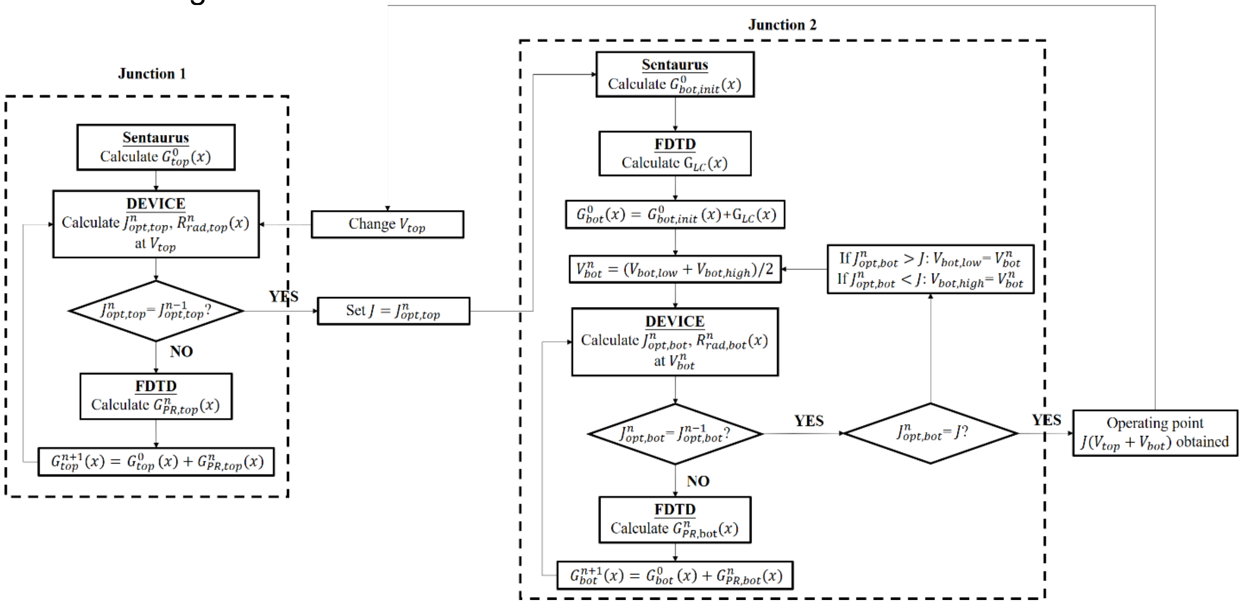

Fig 1. Flowchart for iterative procedure to integrate LC and PR into simulation.

Cell temperature leads to significant difference of cell performance, especially in concentrated photovoltaic (CPV) systems where cell temperature can be above 80 ℃ under concentration. Therefore, it is worthwhile to perform investigation on temperature dependence of LCE. Based on our model, influence of temperature on coupling efficiency is studied in detail in Fig. 2 under different applied voltage. The cell temperature was varied from 300 K to 400 K. Under 300 K, LCE for the cell operating at MPP is about 9% while at higher temperature the coupling efficiency dropped significantly. Especially, LCE at MPP decreased to 6% at 400K. In additional to a down shift, a left shift was also observed.

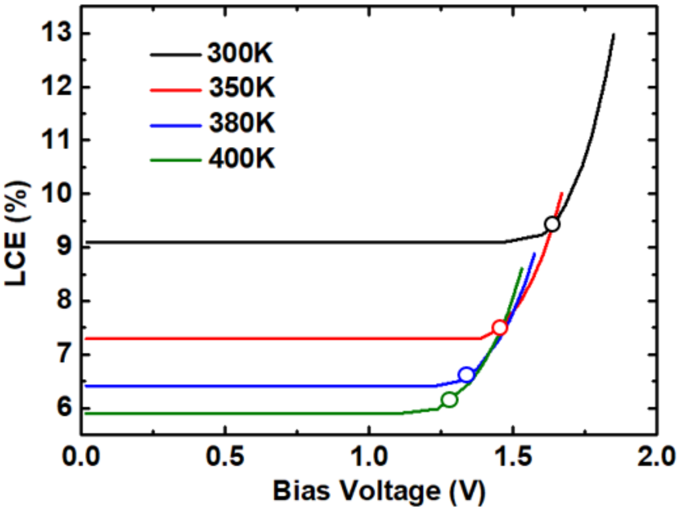

Fig 2. Temperature dependence of luminescent coupling efficiency

The second important factor that influence LCE is light intensity. In practical, solar irradiance can be varied in a wide range during different time of day and year. Again the impact of light intensity will be more significant in a CPV system. Fig.3a) illustrated the influence of irradiance on coupling efficiency. The light intensities were changed from 1 sun to 500 suns and LCE at MPP doubled from ~ 9% to ~ 24% (circles in Fig. 3a)), indicating a much stronger coupling effect between the two junctions under high illumination. For clarity, we repeated the simulation in and similar results for emission efficiency were illustrated in Fig. 3b) with MPP circled out. One important feature can be extracted when light intensity increases: the relative position between “valley” in EE curve and MPP changes significantly. Under 1 sun condition, MPP lies in the “valley”. However, under 100 sun and 500 sun, MPP moves far away from the valley and locates in the rapid increasing region.

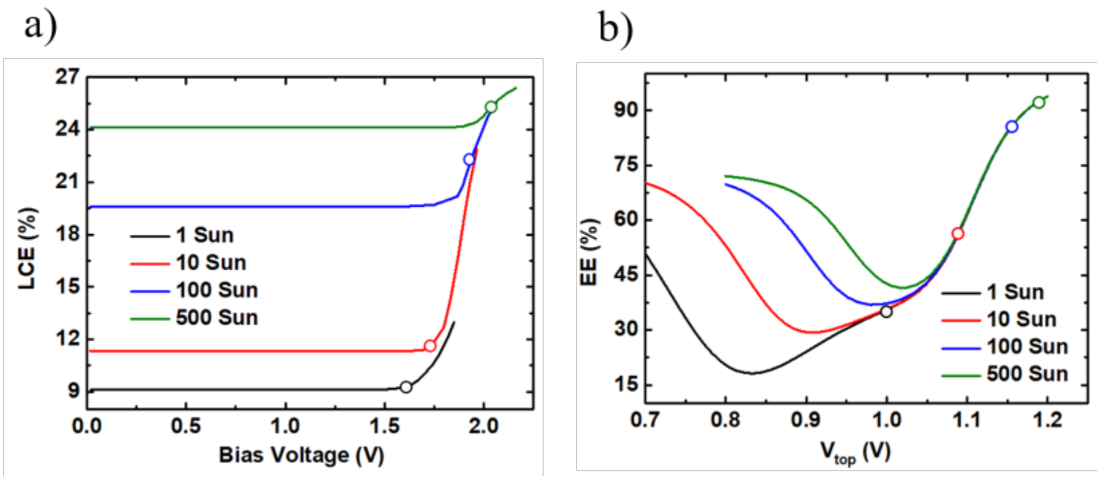

Fig. 3. Light Intensity dependence of LCE and EE

B. Experimental measurement of luminescent coupling

A measurement process was designed. Fig 4 is a schematic design of our system to develop a methodology and measure LC in triple junction cells. The method uses three LED DC light sources corresponding to the bandgaps of the three junctions. By adjusting the light intensities, the cell can be tuned into different junction limit conditions. For simplicity, we made J3 the limit junction, while making J1 generate a much larger photocurrent compared with other two junctions. Then a small signal pulsed light was applied on J2. The MJ cell can then be represented by an equivalent circuit model with the necessary components illustrated in Fig. 5.

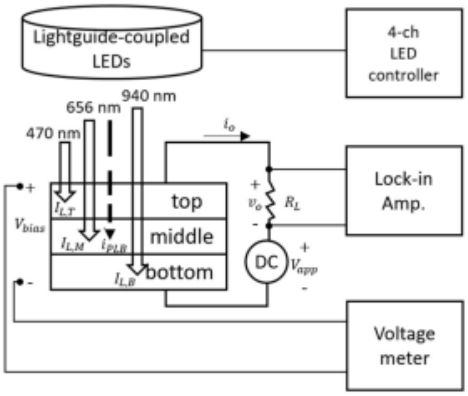

Fig 4. Schematic of luminescent coupling characterization

A DC circuit model was first developed. For each junction, a current source represents the photocurrent generated by LED light. Two diodes with ideal factor n=1 and n=2 represents the electric induced recombination. A current controlled source was implemented in the same junction to represents photo induced recombination. The luminescent coupling current was also represented as current controlled source, by the summation of the electric induced recombination and light induced recombination. The small signal analysis circuit was created in the similar way. Noted the small signal circuit only contain the small signal current source, and the diodes became resistors with certain value. Based on small signal analysis, a relationship between output signal and pulsed light signal can be expressed as:

$$\boldsymbol{i_o} = \frac{[(\mathbf{1}-\boldsymbol{k})\boldsymbol{r_m} + \boldsymbol{\eta^{M,B}}\boldsymbol{r_b}]}{[\boldsymbol{R_L} + \boldsymbol{r_t} + (\mathbf{1}-\mathbf{k})\boldsymbol{r_m} + (\mathbf{1}+\boldsymbol{\eta^{M,B}})\boldsymbol{r_b}]}\boldsymbol{i_{PLB}} \tag{13}$$

Where all the small signal resistors can be obtained by measuring J-V curve of reference cells.
The $\boldsymbol{i_o}$ and $\boldsymbol{i_{PLB}}$ can be measured by changing junction limit conditions.

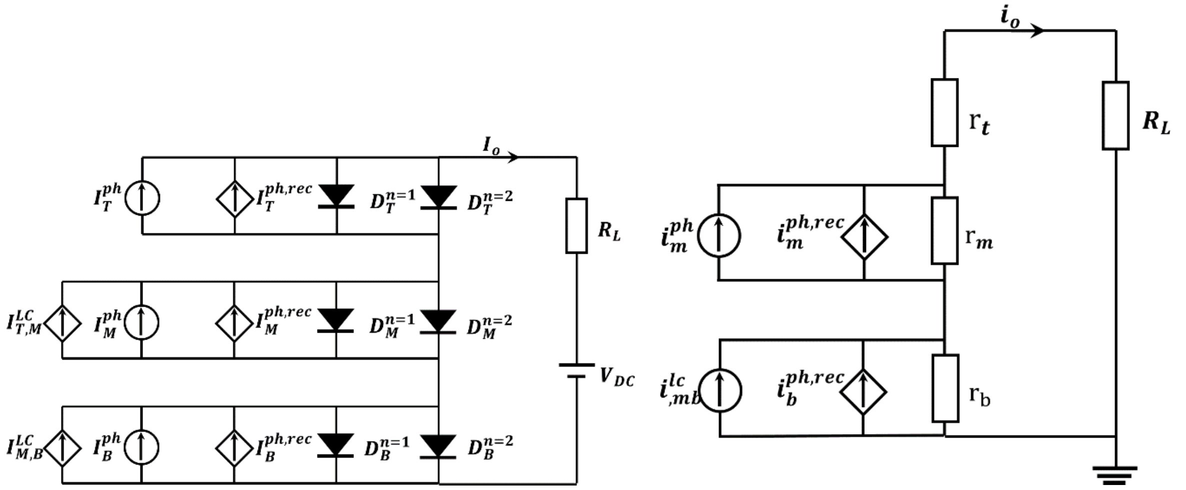

Figure 5. Triple Junction model for luminescent coupling

Photoluminescence (PL) and electroluminescence (EL) measurements were conducted to obtain the parameter k. We define a constant portion of light induced recombination current will emitted through front side of the cell and detected by PL setup, the portion can be determined as:

$$\boldsymbol{\gamma} = \frac{\boldsymbol{J_{PL}}}{\boldsymbol{J_{PL,rec}}} = \frac{\boldsymbol{J_{PL}}}{\boldsymbol{kJ_{ph}}} = \frac{\boldsymbol{J_{EL}}}{\boldsymbol{J_{EL,rec}}} \tag{14}$$

$$\boldsymbol{J_{sc}} = (\mathbf{1}-\boldsymbol{k})\boldsymbol{J_{ph}} \tag{15}$$

Thus:

$$\boldsymbol{J_{PL}} = \boldsymbol{\gamma}\frac{\boldsymbol{k}}{\mathbf{1}-\boldsymbol{k}}\boldsymbol{J_{sc}} \tag{16}$$

The parameter $\boldsymbol{\gamma}$ can be measured with EL measurement.

A setup for LC effects characterization was built, the photo is shown in Fig 6.

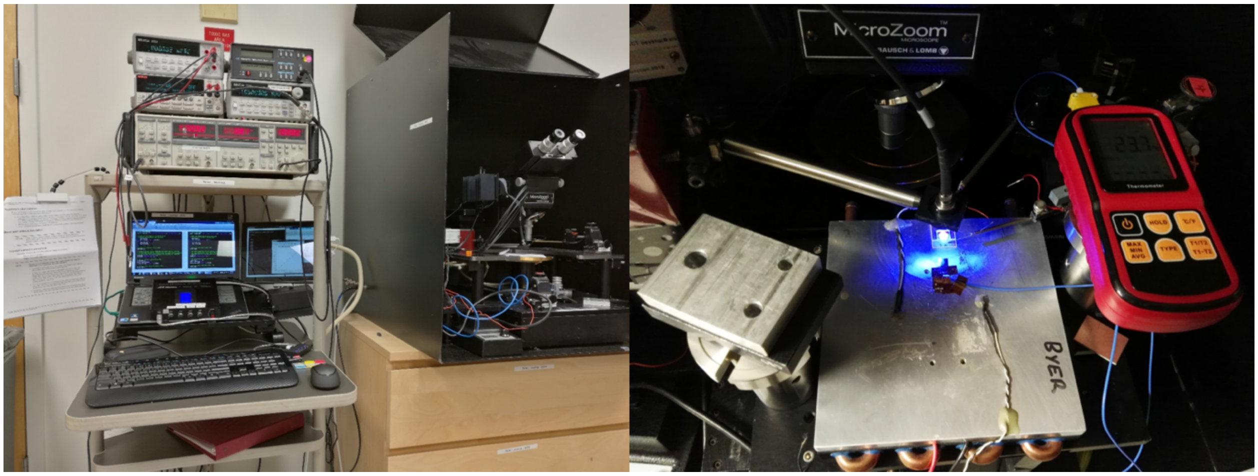

Fig 6. Setup for LC effect measurement

The characterization method we have been developing is based on small signal response to characterize the LC effects in typical industry CPV solar cells. The small signal response can conduct the measurement on the fixed operating point of the cell under certain bias voltage spectral condition and temperature. The measurement result on bias voltage and irradiance dependence of LC effects was measured as is shown in Fig 7 a). We also used the conventional method to confirm the temperature dependence of LC effects, as shown in Fig 7 b).

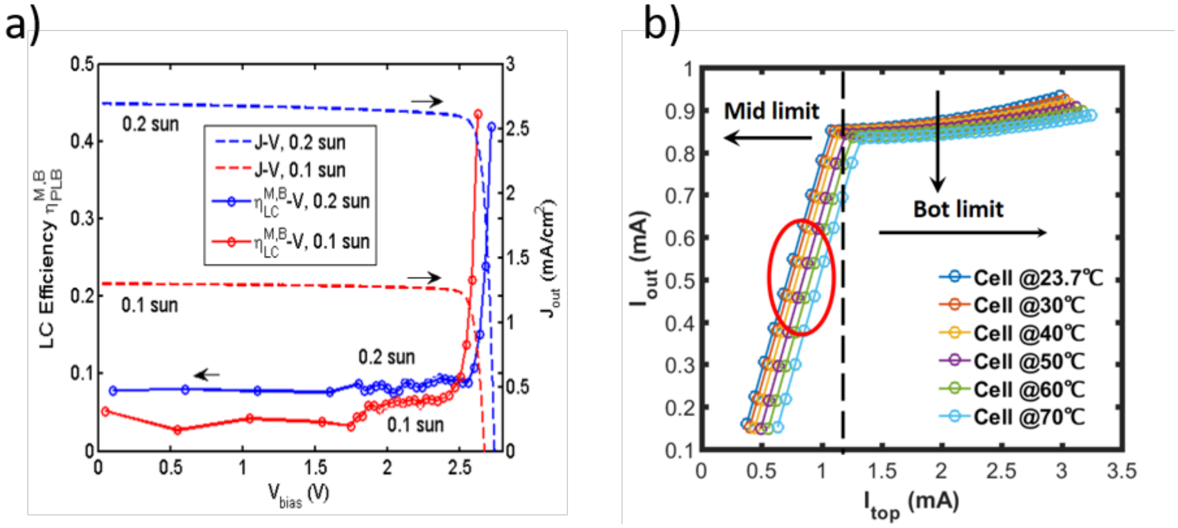

Fig 7. a) bias voltage-light intensity and b) temperature dependence of LC effects

B. Radiative Cooling

1. Background

The heating of the solar cell has adverse consequences on both its performance and reliability [1]. The conversion efficiency of the solar cell deteriorates at elevated temperatures. For example, for crystalline silicon solar cells, every 1°C temperature rise leads to a relative efficiency decline of about 0.45% [2]. In addition, the aging rate of a solar cell array doubles for every 10 °C solar cell temperature increase [3]. In concentrated photovoltaic systems (CPV) [4], the thermal management is even more critical. Therefore, it is extremely important to develop solar cell cooling techniques to keep the cell operating temperature as low as possible.

Existing solar cell cooling strategies, including conduction of heat to dissipation surfaces [5], forced air flow [6], water cooling [7] and heat-pipe-based systems [8,9], have been mainly focused on engineering the non-radiative heat transfer accesses of solar cells using heat conduction or convection approaches. Some of these conductive or convective cooling techniques either need extra energy input or increase the system complexity. On the other hand, radiative heat exchange plays a significant role in the thermal balance of the solar cell. A solar cell is heated up by the sun, and moreover it naturally faces the sky, and therefore can radiate some of its heat out as infrared radiation. Therefore, complementary to non-radiative approaches, it is also of importance to explore the possibilities of using the photonic approach to engineer the radiative heat transfer access of solar cells for thermal management.

Recently, there is an emerging interest to design the thermal radiation property of outdoor structures for cooling purposes [10-12]. This radiative cooling approach is based on the fact that any sky-facing structure naturally has radiative access to the cold universe through the Earth’s atmosphere’s transparency window between 8 and 13 μm [10]. Moreover, since solar cells under sunlight are typically operating above the ambient air temperature, thermal emissions outside the atmosphere transparency window in the entire wavelength range between 4-20 microns also help in radiative cooling. Based on this concept, we have recently designed and demonstrated a photonic structure that is transparent in the solar wavelength range, yet behaves as a blackbody in the thermal wavelength range [11,12]. Such radiative cooling structures can that be used to cool the solar absorber underneath. However, the effects of radiative cooling on practical solar cell systems including concentrated photovoltaic system and flat silicon solar panels were unclear.

2. Results and Discussion

We have examined radiative cooling effects on refractive concentrator photovoltaic systems and silicon solar cells. Our main results can be summarized in four parts:

1. We examined the infrared transmission properties of commercial refractive (Fresnel) concentrators. The optics of commercial refractive (Fresnel) concentrators prevent application of radiative cooling concepts due to strong mid-IR absorption (4-12μm) required to effectively radiate blackbody radiation from the cells and provide cooling.
2. We identified that the existing crystalline silicon solar cells are not ideal for thermal management purpose: Existing crystalline silicon solar cells have sub-

optimal thermal radiation for radiative cooling purpose, and significant sub-band gap solar absorption induced parasitic heat generation.

3. We experimentally verified radiative cooling effects on crystalline silicon solar cells and developed thermal modeling in good agreement with experimental data.
4. We proposed a photonic design as retrofit for cooling of existing silicon solar panels. Such photonic structures can strongly enhance the radiative cooling in the infrared wavelength and simultaneously suppress the sub-band gap absorption induced parasitic heat generation.
5. We measured and modeled the temperature drop across the cover glass and EVA elastomer used to attach the cover glass and found this to be ~3.5°C. Finding an elastomer with higher thermal conductivity could reduce this temperature increase and enhance the radiative cooling effect, improving overall cell and module efficiency by as much as 1.5% absolute.

a. Radiative cooling effect in refractive concentrators

To study the radiative cooling effect on existing refractive concentrator photovoltaic systems, we examined the infrared transmission properties of commercial refractive (Fresnel) concentrators (Fig. 8). In the infrared wavelength range between 2 – 20 μm, the transmission spectra of the two Fresnel lens are shown in Fig. 8. Both lenses show very little transmission in the required thermal wavelength range. As a result, the optics of the three commercial refractive (Fresnel) concentrators we examined prevent application of radiative cooling concepts due to strong mid-IR absorption (4-12μm) required to effectively radiate blackbody radiation from the cells and provide cooling.

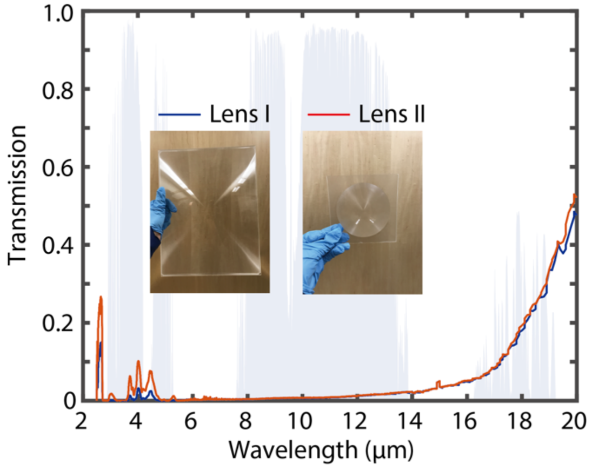

Fig 8. Experimentally measured transmission spectra of two concentrator lens over the infrared wavelength.

Investigation of alternative materials for the concentrator lenses produced only undesirable options—materials with reasonable mid-IR transmission for cooling only had about 30-40% visible transmission, thus reducing incident sunlight by > 50%. While our investigation was somewhat limited, our work suggests that the only viable concentrator system that can incorporate radiative cooling must utilize reflective optics.

b. Radiative cooling opportunity in existing C-Si solar cells.

Since it was impossible to explore radiative cooling in the experimental concentrator systems we had available, we were encouraged to examine c-Si cells where there was no concentration. We experimentally examined solar absorption and thermal emission properties of typical commercial crystalline silicon solar cells. Since in practice in a photovoltaic module a solar cell is always encapsulated, we also encapsulated the solar cell by sandwiching it with two 0.46 mm thick ethylene-vinyl acetate (EVA) joint interlayers, with a 3.2 mm thick glass as front cover and a 0.5 mm thick back sheet layer made of polyvinyl fluoride. The materials and parameters for the encapsulation layers were chosen according to commercial solar panel standards.

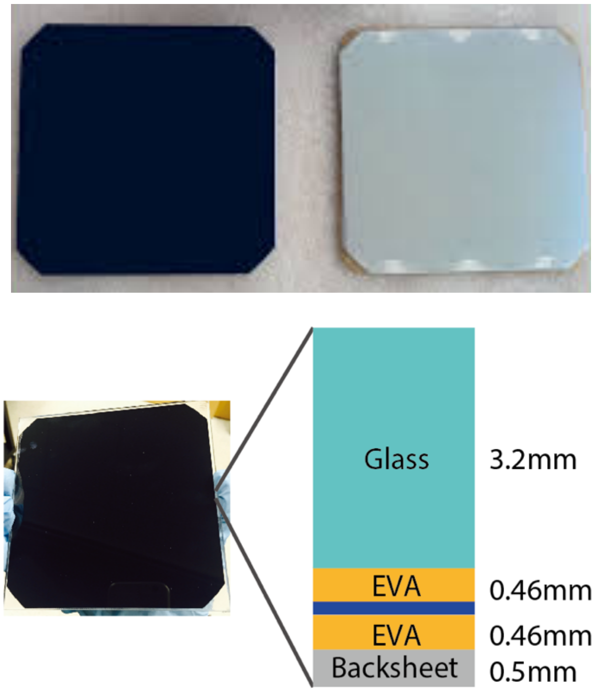

Fig 8. Top: Photos of back-contact crystalline silicon solar cell. Bottom: Photo and schematic of the encapsulated solar cell. Photo (left) and a cross-section schematic (right) of a solar cell with encapsulation, made of cell I, with a 3.2 mm front glass cover, top and bottom 0.46 mm EVA film and a 0.5 mm back sheet.

The solar absorption and thermal emissivity spectra of the bare cells and the encapsulated cell are experimentally characterized and shown in Fig, 9. In the solar wavelength region, the bare cell show strong light absorption from 0.3 to 1.1 μm, where the photon energy is above the silicon band gap, as expected. In the wavelength range between 1.1 to 1.8 μm, the bare cell shows significant sub-band gap absorption, even though photons at these wavelength ranges have energy below the silicon band gap. Such a strong sub-bandgap absorption is in contrast with measured data on a bare silicon wafer with planar anti-reflection coating and metallic back reflector, most likely due to the presence of metal contacts and heavily doped regions in the cells. The sub-bandgap absorption may be further enhanced by the light trapping effects induced by surface textures. From the measured absorption spectra, under AM1.5 illumination, the sub-band gap absorption of the bare cell is calculated to be 85 W/m^2, respectively. Such sub-band gap absorption represents a parasitic heat source that does not contribute to current generation.

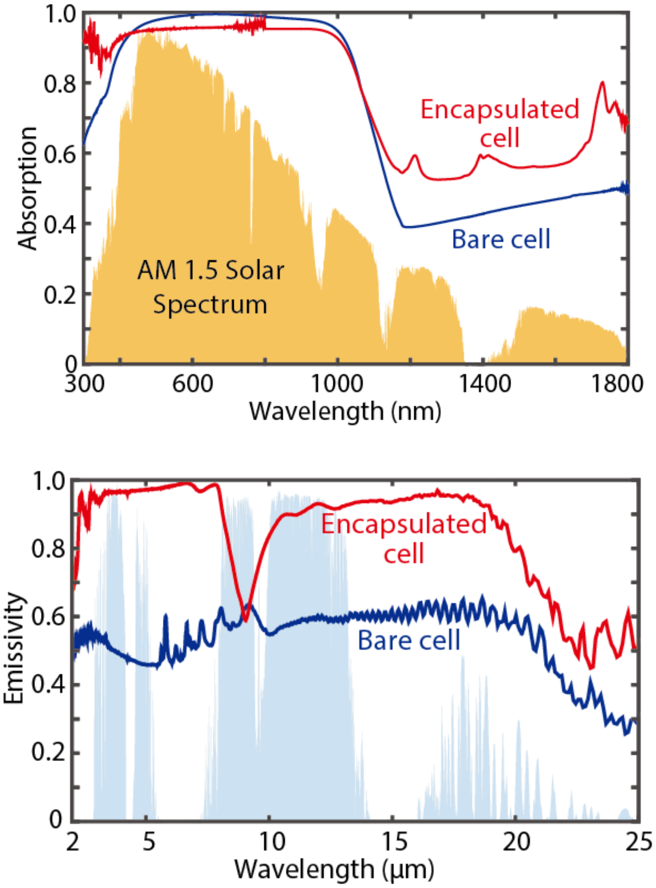

Fig 9. Top: Experimentally measured solar absorption spectra of the bare cell and the encapsulated cell, with the normalized AM1.5 solar spectrum plotted for reference. Bottom: Experimentally measured emissivity spectra of the bare cell and the encapsulated cell over the infrared wavelength, with atmosphere transmittance plotted as the shaded area.

Compared to the bare cell, the encapsulated cell shows an even stronger absorption in the sub-bandgap as well as UV wavelength range. The encapsulated cell has a sub bandgap absorption of 110W/m^2 for the AM 1.5 illumination, which is significantly higher than that of the bare cell. This is due to the fact that EVA strongly absorbs UV light with wavelength shorter than 0.375 μm and slightly absorbs in the near infrared regime. Such absorption can lead to excess heat generation while also degrade the EVA, reducing the lifetime of the solar panels. Therefore, for cooling purposes, and also to enhance the lifetime of encapsulated cell, it is beneficial to suppress the sub-band gap and UV absorption of the solar panel while preserving or even enhancing the absorption of the solar cell in the wavelength range of 0.375-1.1 μm.

In the infrared wavelength range between 2 – 25 μm, the emissivity spectra of the bare solar cells and encapsulated cell are shown in Fig. 9. Both the bare and the encapsulated cells show strong absorption and hence strong thermal emission in the thermal wavelength range. For the bare cells, although silicon is a weak absorbing material in this regime, the presence of highly doped silicon region, metal contacts and anti-reflection layers, usually made with SiN or SiO_2, all of which have non-zero absorption in the thermal wavelength range, together with the light trapping effect, result in significantly large absorptivity/emissivity of the solar cells in the thermal wavelength range. For the encapsulated cell, its thermal emissivity is even higher in the most of the wavelength range between 2-25 μm, and is mainly determined by the 3.2mm thick front glass layer which contains 70%-80% silica. As shown in Fig. 9, the measured emissivity spectrum of the encapsulated cell is very similar to the measured or calculated emissivity spectra of fused silica.

As a result, the existing crystalline silicon solar cell has strong sub-bandgap absorption in the solar wavelength range, as well as substantial thermal emission in the wavelength range of 2-25 μm. Encapsulation of solar cells, as is required in photovoltaic modules, further enhances the sub-band gap solar absorption and the thermal emission, and in addition enhances the solar absorption in the UV wavelength range.

From the perspective of thermal management, the presence of strong solar absorption in the sub-band gap and UV wavelength range is detrimental since this absorption represents a parasitic heat source. The presence of high emissivity in the thermal wavelength range is beneficial. It is important to note, however, that the thermal emissivity spectra of commercial solar cells, even in the best-case scenario with the encapsulation layer, is sub-optimal.

3. Experimental verification of radiative cooling on solar cells and thermal modeling:

To experimentally verify the radiative cooling effect on solar cells, an outdoor temperature measurement setup was built for characterization of solar cell temperatures during daily the daytime (Fig 10).

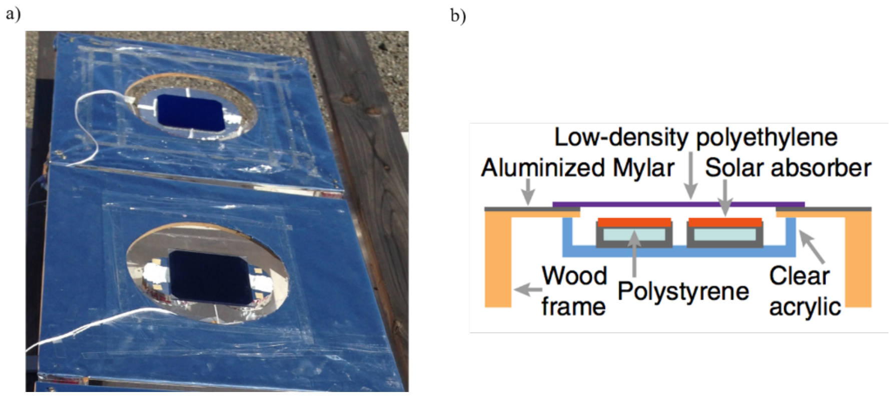

Fig 10. Temperature measurement setup for outdoor measurement

As is shown in Fig 11, the average temperature of the encapsulated cell is 2.8°C lower than bare cell. Such results indicate the effect of radiative cooling: even though the encapsulation process increased total solar absorption of the solar cell, the encapsulated cell still has a lower temperature as compared to the bare cell.

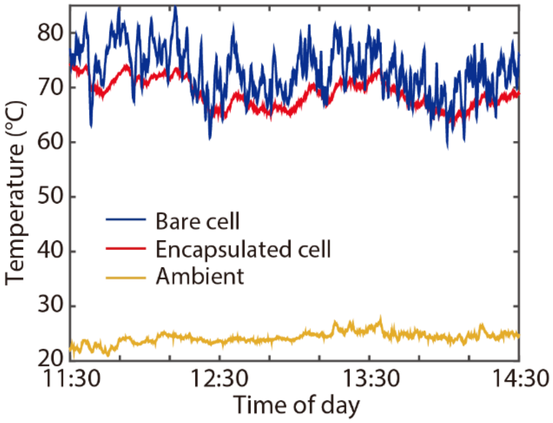

Fig 11. Outdoor temperature characterizations of bare solar cell and encapsulated solar cell: the encapsulated solar cell has an average temperature of 2.8°C lower than the bare cell, demonstrating the radiative cooling effect.

Thermal modeling of solar cell temperatures: The temperature measurement results here can be well accounted by a thermal model, taking solar irradiance, ambient temperature, atmosphere transparency window. We set up a finite-difference-based thermal simulator where we can simulate the temperature distribution across the solar cells in the vertical direction by solving the steady-state heat diffusion equation:

$$\frac{d}{dx}\left[k(z)\frac{dT(z)}{dz}\right]+\dot{q}(z)=0 \tag{16}$$

where $T(z)$ is the temperature distribution across the solar panel. We apply the thermal boundary condition at the top surfaces of the solar panel as:

$$-k(z)\frac{dT(z)}{dz}\Big|_{top}=P_{cooling}(T_{top})+h_1(T_{top}-T_{amb}) \tag{17}$$

to take into account both the radiative cooling effect $P_{cooling}(T_{top})$, as well as additional non-radiative heat dissipation due to convection and conduction, as characterized by $h_1(T_{top}-T_{amb})$. At the lower surface, we assume a boundary condition

$$k(z)\frac{dT(z)}{dz}\Big|_{bottom}=h_2(T_{bottom}-T_{amb}) \tag{18}$$

to characterize the non-radiative heat loss of the lower surface.

Based on the solar absorptivity and thermal emissivity spectra of the encapsulated cell and the photonic cooler, we can first calculate the total solar absorption and radiative cooling power of the solar panels by:

$$P_{sun} = \int_0^\infty d\lambda \cdot I_{AM1.5}(\lambda) \cdot \varepsilon(\lambda, \theta_{sun}) \cdot (1 - r(\lambda, \theta_{sun})) \cdot \cos\theta_{sun} \tag{19}$$

where P_{sun} is the solar absorption power, $I_{AM1.5}(\lambda)$ is the AM1.5 spectrum, $\varepsilon(\lambda, \theta_{sun})$ is the solar absorptivity of the solar cell. $r(\lambda, \theta_{sun})$ is the reflectivity spectrum of the photonic cooler. θ_{sun} is the solar incidence angle. Here we assume the heat is uniformly generated in the solar cell and we can obtain $\dot{q}(z)$ in Eq.1. Meanwhile, the top surface radiative cooling power $P_{cooling}$ can be calculated as:

$$P_{cooling}(T_{top}) = P_{rad}(T_{top}) - P_{atm}(T_{amb}) \tag{20}$$

P_{rad} is the total thermal radiation power by the solar panel and can be calculated as:

$$P_{rad}(T_{top}) = \int d\Omega \cdot \cos\theta \int_0^\infty d\lambda \cdot I_{BB}(T_{top}, \lambda) \varepsilon(\lambda, \Omega) \tag{21}$$

where $\int d\Omega = \int_0^{\pi/2} d\theta \sin\theta \int_0^{2\pi} d\phi$ is the angular integral over the hemisphere.
$I_{BB}(T, \lambda) = \left(2hc^2 / \lambda^5\right) / \left[e^{hc/\lambda K_B T} - 1\right]$ is the spectral radiance of a blackbody at temperature T, where h is the Planck's constant, c is the velocity of light, K_B is the Boltzmann constant.

P_{rad} is the absorbed thermal emission power from the atmosphere and can be calculated as:

$$P_{atm}(T_{amb}) = \int d\Omega \cdot \cos\theta \int_0^\infty d\lambda \cdot I_{BB}(T_{amb}, \lambda) \varepsilon(\lambda, \Omega) \varepsilon_{atm}(\lambda, \Omega) \tag{22}$$

where $\varepsilon_{atm}(\lambda, \Omega) = 1 - t(\lambda)^{1/\cos\theta}$ is the angular-dependent emissivity of atmosphere and $t(\lambda)$ is the atmosphere's transmittance in the zenith direction.

The temperature distribution across the encapsulated cell was simulated in Fig 12. As can be seen, the temperature can be varied by ~3℃ from the surface of the front glass to the cell. The operating temperature of the solar cell is then defined as the spatially averaged temperature inside the solar cell region.

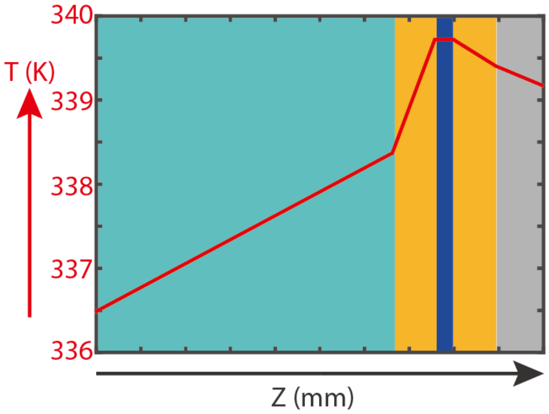

Fig 12. Temperature distribution across encapsulated cell. The green, yellow, blue, and grey region are front glass, EVA, silicon solar cell and backsheet, respectively.

To model the operating temperature of the solar cells during the daytime, we input the experimentally derived absorption/emission data of the bare cells and encapsulated cells, the AM1.5 spectrum weighed to the measured solar irradiance, and the atmosphere transmission for a clear sky at Stanford during the measurement days. The modeled temperatures of both bare solar cells and the encapsulated solar cells are shown in Fig. 6 and Fig. 7, respectively. Good agreements between the modeled temperatures and the experimentally measured temperatures for both the bare cell and the encapsulated cell.

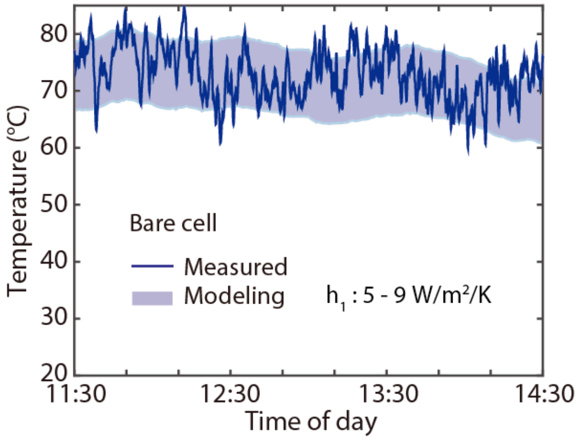

Fig 13. Modeling of steady-state temperature of bare solar cell (blue shaded area) with h_1 value range from 5 to 9 $Wm^{-2} \cdot K^{-1}$, showing a reasonably good agreement with the experimentally measured data.

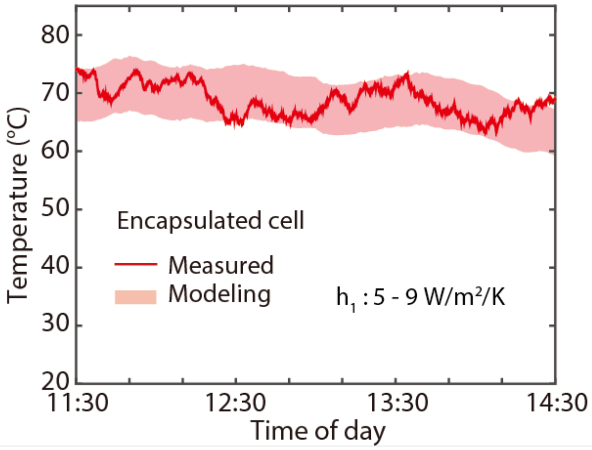

Fig 14. Modeling of steady-state temperature of encapsulated solar cell (red shaded area) with h_1 value range from 5 to 9 $Wm^{-2}\cdot K^{-1}$, showing a reasonably good agreement with the experimentally measured data.

4. Proposed photonic designs for cooling of existing silicon solar panels

We design photonic structures for the thermal management of solar cells by adding a multilayer dielectric stack on top of an existing encapsulated solar panel. This approach can be used as a retrofit: it does not require any modification of existing structures or materials in standard encapsulated cell.

For optimal thermal management purposes, the added photonic structure needs to satisfy the following design criteria as shown in Fig 15. First, in the solar wavelength range, the photonic structure needs to have a tailored transmission/reflection characteristic. In the wavelength range of 0.3 – 0.375 μm and 1.1 – 4 μm, the photonic structure needs to have maximized reflection to reduce the parasitic heat generation. Whereas in the wavelength range of 0.375 – 1.1 μm where photons can be converted into photocurrent, the photonic structure needs to have minimum reflection to reduce the reflection loss. Second, to maximize the radiative cooling performance of the solar cell, the photonic structure needs to have maximized emissivity in the thermal wavelength range beyond 4 μm. In order to satisfy these criteria, we note the following considerations: First, the constituent materials all need to be transparent over the solar wavelength yet some need to be lossy over the thermal wavelength. Second, to create large solar reflection over the sub-band gap wavelength range, materials with large index contrast need to be used. Third, over the thermal wavelength range, many lossy dielectrics such as silica have strong phonon-polariton response which results in a negative permittivity that leads to large reflectivity and hence low emissivity. Therefore, one needs to combine dielectrics with both positive and negative permittivity to avoid the large reflection. Finally, all the materials should be commonly used dielectrics for cost consideration and should be amenable to large-area fabrication. Taking into account all these considerations, for our multilayer design we choose to use the dielectric materials of silica, alumina, titania and silicon nitride.

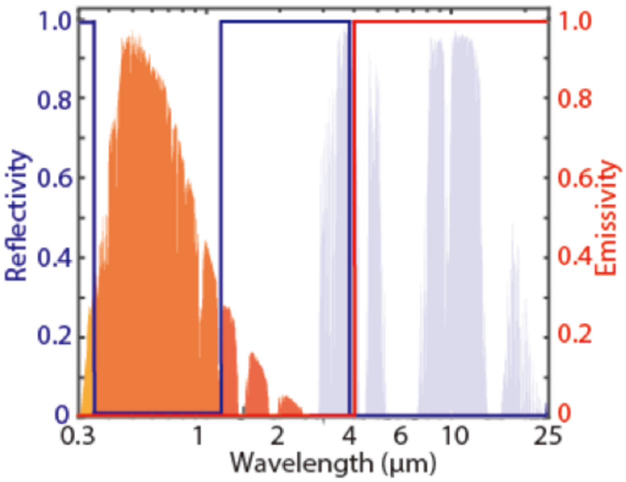

Fig 15. The ideal reflection (blue) and emissivity (red) spectra of a photonic cooler, with the normalized AM1.5 solar spectrum and atmosphere transmittance plotted as the orange and the light blue shaded areas. The wavelength is plotted with a logarithmic scale for clarity.

The photonic cooler design we proposed is schematically shown in Fig. 16. The photonic cooler is on a glass substrate representing the top layer of an encapsulated solar cell, consists of alternating layers of Al_2O_3/SiN/TiO_2/SiN with aperiodic arrangement of thickness, with a single top layer of SiO_2 for anti-reflection purpose. The use of aperiodic structure, as opposed to a periodic structure, serves to minimize the reflection oscillation in the wavelength range of 0.375 to 1.1 μm.

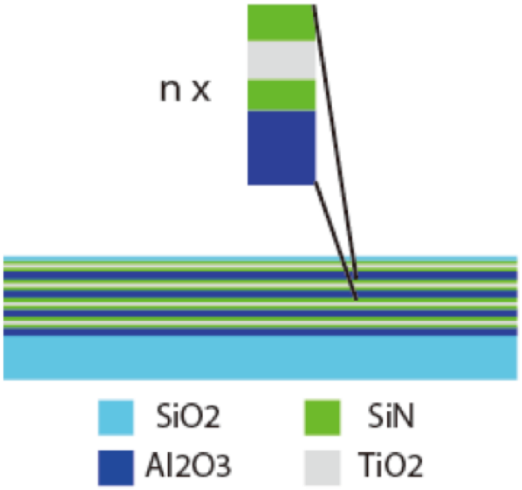

Fig 16. Schematic of a photonic cooler made of multilayer dielectric stack, with n sub-layers. Each sub-layer is made of Al_2O_3/SiN/TiO_2/SiN, and a single SiO_2 layer on top. The photonic cooler is on a glass substrate. The structure thickness is aperiodic for optimized performance.

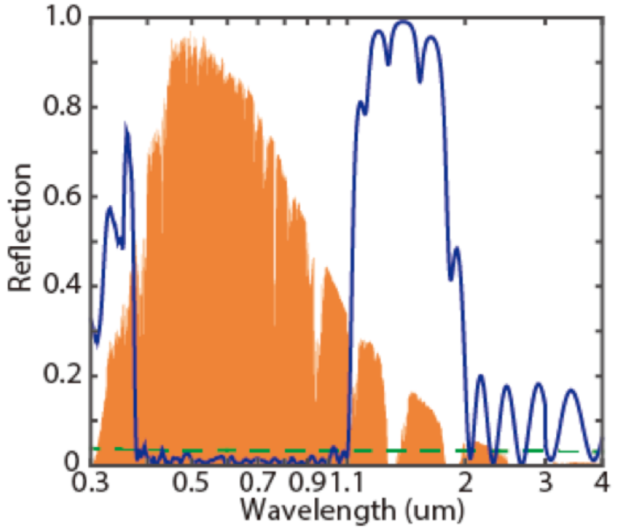

Fig 17. Reflection spectrum of the photonic cooler (blue). The reflection spectrum of a glass substrate without a photonic cooler (dashed green) is plotted for reference. The wavelength is plotted with a logarithmic scale for clarity.

The calculated solar reflectivity and thermal emissivity spectra of this structure are shown in Fig. 17 and 18, respectively. Over the solar spectrum, the structure exhibits strong reflection in the sub-band gap and UV wavelength range. In the wavelength range of 0.375 to 1.1 μm, this cooler also serves as broadband anti-reflection coating and enhances the solar transmission, as compared to the case without coating (dashed green curve in Fig. 10). In this wavelength range, the transmitted power through this photonic cooler is calculated as 772.6 W/m^2, which is more than the case without the photonic cooler 755.5 W/m^2. In the wavelength range between 1.3 and 1.8 micron, the cooler structure shows a reflectivity that is near unity, which is important in suppressing the parasitic absorption and heat generation from part of the solar spectrum that is below the silicon band gap. Lastly, this cooler also shows a broadband high emissivity over the thermal wavelength (Fig. 11). In particular, over the 8-13 μm atmosphere's transparency window, this cooler shows remarkably high emissivity, as opposed to silica,

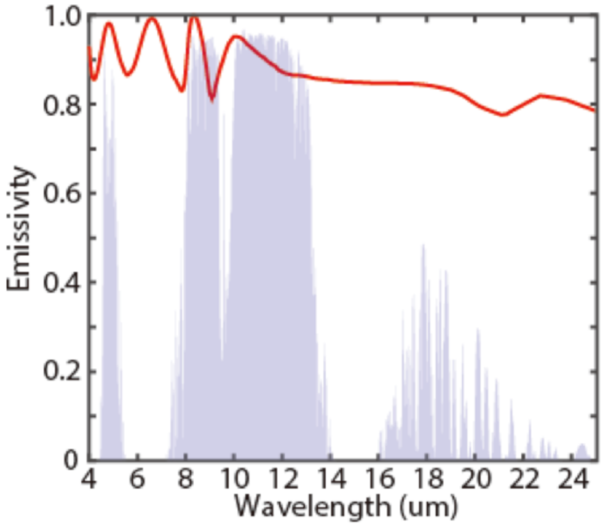

Fig 18. Emissivity spectra of the photonic cooler over the infrared wavelength, with a realistic atmosphere transmittance plotted as the shaded area.

The cooling effect from this photonic cooler is shown in Fig. 19. The temperature across a silicon solar panel can be significantly reduced by applying a photonic cooler on the top surface. The cell operating temperature is also calculated by spatially averaging the temperature inside the solar cell region. As a result, the cell operating temperature can readily be lowered by 5.7K with current photonic cooler design and by 8.6K with an ideal photonic cooler (Fig. 11). For a 22% efficiency silicon solar cell with a temperature coefficient of 0.45%, this 5.7K temperature reduction can provide an absolute efficiency improvement of 0.56%, without the need of modifying the current solar panel configuration. Together with the solar transmission enhancement in the wavelength range of 0.375 to 1.1 µm, the overall absolute efficiency improvement is estimated to be around 1%.

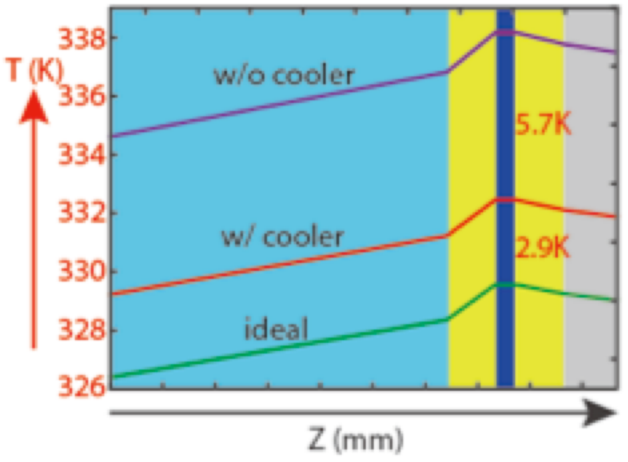

Fig 19. Under AM1.5 illumination, simulated temperature distribution across a solar panel without a photonic cooler (purple), with a photonic cooler (red), and in the ideal situation (green), respectively. The top and bottom ambient temperature are both 298 K.

Applying a photonic cooler on the silicon solar panel can lower down the operating temperature by 5.7K in a typical outdoor condition.

While nominally planned for the second year, initial testing to demonstrate radiative cooling was initiated and a preliminary cooling effect measurement was conducted for a low CPV system. As an initial step, we used poly-silicon cells with silica layer on the surface for the outdoor test because we could procure smaller size, electronically current compatible with our measurement system. We tried various approaches to cut down the size of high-efficiency, Sun Power c-Si cells to be current compatible, but all efforts resulted in serious performance degradation. We need permission to purchase a high current source that will integrate with our outdoor test facility and enable demonstration of radiative cooling in high efficiency c-Si cells. The cell we used with and without cooling layer was shown in Fig 6 a). After the encapsulation the cells were mount on the CPV test module for testing. The setup was shown in Fig 20 b).

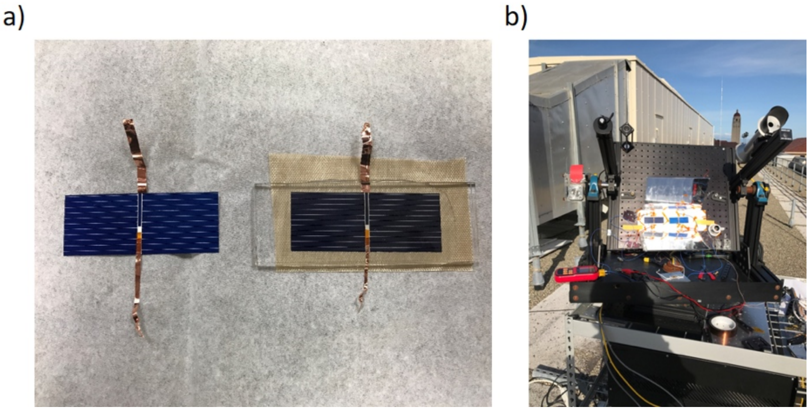

Fig 20. Comparison of cells with and without cooling layer

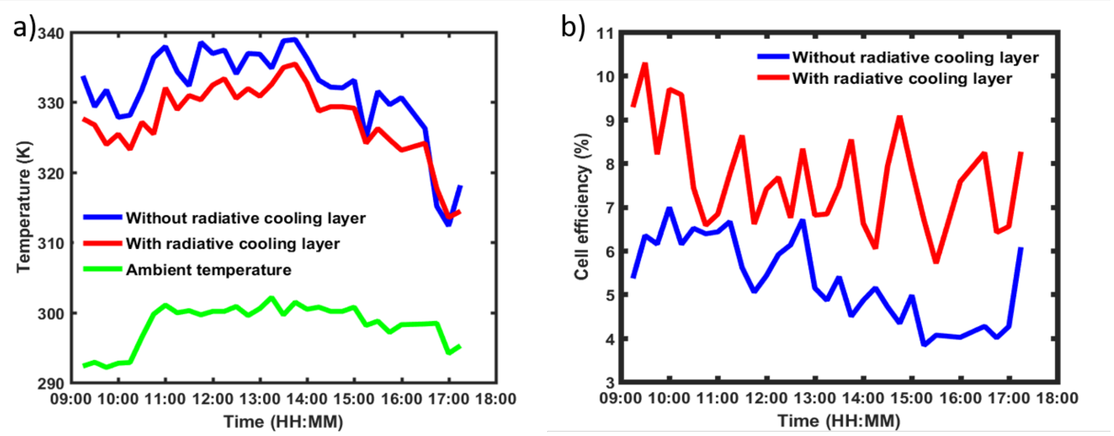

Fig 21. Comparison of a) temperature and b) efficiency of cells with and without cooling layer 2suns were concentrated on the silicon cell. A temperature reduction greater than 4℃ was observed, and a higher daily efficiency was confirmed

C. Conclusions:

The major conclusions of the program are summarized below:

Earlier numerical models for luminescent coupling efficiency were at typically two fixed operating point—Open Circuit Voltage and Shor Circuit Current. We developed a numerical model to explore the dependence of luminescent coupling efficiency over a broad range of operating and environmental conditions. We developed a novel experimental facility using four different colored LEDs to change the operating point of individual cells in a multi-junction stack to experimentally measure the luminescent coupling between different cells. This system was used to confirm the predicted dependence of luminescent coupling on multi-junction cell design parameters from our model.

We examined the infrared transmission properties of commercial refractive (Fresnel) concentrators and found that none of the existing refractive concentrators enable radiative cooling due to their strong mid-IR absorption (4-12µm). Good transmission in this region is required to effectively radiate blackbody radiation from the cells and provide cooling. First, existing c-Si solar cells have sub-optimal surface treatment for optimal radiative cooling and second, they have significant sub-band gap solar absorption producing unintended parasitic heat generation. Both of these effects can be mitigated by providing an appropriate silica layer on top of the encapsulate layer and utilizing a higher thermal conductivity elastomer adhesive between the solar cell and cover glass encapsulant. Finally, an additional multi-layer film like the common AR films can be added to selectively reflect near-IR (1.3-4µm) that heat the cell. The combination of optimized radiative cooling and elimination of parasitic IR radiation could reduce cell operating temperature by up to 15°C and increase overall cell and module efficiency by as much as 1.5% absolute.

D. Budget and Schedule:

The total budget for the 2-year program was $700,000, of which $118,056 was the proposed cost share and $140,000 was for a subcontract to NREL. The intended start date was October 1, 2016 and ending date September 30, 2018. The program was ended after one year, thus the budget amounts were half of the above figures. Since there was still considerable funding remaining, a 3-month no-cost extension was allowed. The total expenditures were $251,153, of which $191,479 was the Federal Share and $59,674 was the Stanford Cost-share or 23.8%, roughly 1.5X the proposed Cost-share, thus leaving $48,874 unspent, even after the extension. The biggest issues with both performance and spending were due to slow and difficult contractual agreements. While the official start date was October 1, a signed contract and Stanford accounts were not established until mid-November, by which time all of the students were already committed to other projects, meaning virtually nothing beyond discussions occurred until the first week of January 2017. The NREL subcontract was even much further delayed to their payment requirements and a final contract was not signed until June 29, 2017, giving them 3 months rather than 12 to complete their technical tasks and spend the available funding. This resulted in restructuring and moving some of the tasks to Stanford since NREL was unable to contribute until the program was nearly ended.

E. Path Forward;

There would appear to be two quite separate paths to follow work from this program.

First, to investigate both the performance gains and increased complexity and cost for incorporating the mid-IR reflective layers, higher thermal conductivity elastomer encapsulant material and uppermost silica layer for radiative cooling in both flat plate and low concentration c-Si solar panels

Second, to utilize the model and test facility for luminescent coupling developed in the program and apply this to the new effort on perfectly matching 3-4-5 junction cells with a new electrolyzer system with low cost electrodes based upon the world record results (>30% Solar to Hydrogen conversion) achieved using 3-juntion solar cells to match an existing electrolyzer system, but which utilizes very costly Pt electrodes. A system with low cost electrodes and perfectly matching solar cell could provide the necessary cost and efficiency combination to make hydrogen generation and attractive approach for both energy storage and fuel for transportation systems.

F. Patents:

None filed

G. Publications/Presentations:

James Harris, “Heterojunctions and Epitaxy: The Foundations of Photonics”, *iNOW Summer School*, Würzburg, Germany, August 1, 2016 (*plenary*)

Zheng Lyu, Muyu Xue, Junyan Chen, Jieyang Jia, Shanhui Fan, James Harris, “

Systematic Thermalphotovoltaic Solar Cell Optimization”, *2017 IEEE 44th Photovoltaic Specialists Conference (PVSC)*, Washington DC, June 2017.

Jia, Jieyang, “Voltage Enhancement In Multijunction Solar Cells and their Application to Water Splitting”, PhD dissertation, Stanford University, June 2017

Jia, Jieyang, Linsey C. Seitz, Jesse D. Benck, Yijie Huo, Yusi Chen, Jia Wei Desmond Ng, Taner Bilir, James S. Harris, and Thomas F. Jaramillo. "Solar water splitting by photovoltaic-electrolysis with a solar-to-hydrogen efficiency over 30%." *Nature Communications,* **7**, 13237, October 2016.

H. References:

1. Dupré, O., Vaillon, R. & Green, M. A. Thermal Issues in Photovoltaics and Existing Solutions. Therm. Behav. Photovolt. Devices 1–28 (2017).
2. Skoplaki, E. & Palyvos, J. A. On the temperature dependence of photovoltaic module electrical performance: A review of efficiency/power correlations. Sol. Energy 83, 614–624 (2009).

3. Otth, D. H. & Ross, R. G. Assessing photovoltaic module degradation and lifetime from long term environmental tests. in 29th Annual Technical Meeting of the Institute of Environmental Sciences 121–126 (1983).

4. Kurtz, S. Opportunities and Challenges for Development of a Mature Concentrating Photovoltaic Power Industry Opportunities and Challenges for Development of a Mature Concentrating Photovoltaic Power Industry. Tech. Rep. NREL/TP-52, 43208 (2012).

5. Royne, A., Dey, C. J. & Mills, D. R. Cooling of photovoltaic cells under concentrated illumination: a critical review. Sol. Energy Mater. Sol. Cells 86, 451–483 (2005).

6. Teo, H. G., Lee, P. S. & Hawlader, M. N. A. An active cooling system for photovoltaic modules. Appl. Energy 90, 309–315 (2012).

7. Moharram, K. A., Abd-Elhady, M. S., Kandil, H. A. & El-Sherif, H. Enhancing the performance of photovoltaic panels by water cooling. Ain Shams Eng. J. 4, 869–877 (2013).

8. Akbarzadeh, A. & Wadowski, T. Heat pipe-based cooling systems for photovoltaic cells under concentrated solar radiation. Appl. Therm. Eng. 16, 81–87 (1996).

9. Zhang, Y. et al. Efficiently-cooled plasmonic amorphous silicon solar cells integrated with a nano-coated heat-pipe plate. Sci. Rep. 6, 24972 (2016).

10. Raman, A. P., Anoma, M. A., Zhu, L., Rephaeli, E. & Fan, S. Passive radiative cooling below ambient air temperature under direct sunlight. Nature 515, 540–544 (2014).

11. Zhu, L., Raman, A., Wang, K. X., Anoma, M. A. & Fan, S. Radiative cooling of solar cells. Optica 1, 32 (2014).

12. Zhu, L., Raman, A. P. & Fan, S. Radiative cooling of solar absorbers using a visibly transparent photonic crystal thermal blackbody. Proc. Natl. Acad. Sci. U. S. A. 112, 12282–7 (2015).